Proceedings of the
Annual Stability Conference
Structural Stability Research Council
Atlanta, Georgia, April 21-24, 2020

A geometrically exact curved thin-walled beam finite element accounting for cross-section deformation

Nuno Peres[1], Rodrigo Gonçalves[2], Dinar Camotim[3]

Abstract
This paper proposes a new geometrically exact beam formulation and ensuing finite element implementation that can handle naturally curved thin-walled members susceptible to global-distortional-local cross-section deformation. The configuration of each cross-section is described by a position vector, a rotation tensor (parameterized using the so-called rotation vector) and arbitrary cross-section deformation modes complying with Kirchhoff's thin plate assumption, meaning that the deformation modes of Generalized Beam Theory can be straightforwardly incorporated. The finite element is obtained by interpolating the independent kinematic parameters using Hermite cubic polynomials. Besides handling large displacements and finite rotations, combined with cross-section deformation, the element is also capable of performing linear stability analyses (of curved members). The accuracy and efficiency of the proposed finite element is demonstrated through several illustrative numerical examples. For validation and comparison purposes, shell finite element model results are provided.

1. Introduction

Most of the current research requiring the computational modeling of thin-walled members susceptible to cross-section deformation is shell finite element-based, even though higher-order beam theories, such as Generalized Beam Theory (GBT), can be employed with significant advantages. However, the application of GBT to naturally curved members is still in its early stages. The first linear (first-order) GBT formulation and finite element implementation for members with circular axis was developed by Peres et al. (2016), using cylindrical coordinates. This formulation was subsequently improved to obtain more rational cross-section deformation modes (for curved members) and a mixed displacement-strain finite element was developed (Peres et al. 2018a, 2018b, 2020). In spite of the important results achieved — for instance, it was shown that complex local-distortional phenomena can occur even in linear problems —, the extension of this formulation to the geometrically non-linear case is far from trivial (even to linear stability analyses), not to mention the generalization to arbitrary initial configurations. Moreover, it is well

[1] PhD Student, CERIS and Departamento de Engenharia Civil, Faculdade de Ciências e Tecnologia, Universidade Nova de Lisboa, Portugal <nr.peres@campus.fct.unl.pt>
[2] Associate Professor, CERIS and Universidade Nova de Lisboa, Portugal <rodrigo.goncalves@fct.unl.pt>
[3] Full Professor, CERIS, Instituto Superior Técnico, Universidade de Lisboa, Portugal <dcamotim@civil.ist.utl.pt>

known that GBT is not suitable to handle moderate to large displacements (particularly moderate rotations), since its kinematic description does not involve true rotations and the bending terms are always assumed to be small.

The so-called geometrically exact beam theory is specifically tailored to handle large displacements and finite rotations. The concept, pioneered by Reissner (1972) and Simo (1985), owes its name to the fact that no geometric simplifications are introduced besides the assumed kinematics. This theory (and its finite element implementation) has been continuously improved to include cross-section deformation as additional DOFs. Torsion-related warping was first included by Simo & Vu-Quoc (1991) and subsequently used by other authors (Gruttmann et al. 2000, Atluri et al. 2001). Petrov & Géradin (1998) introduced distortional and warping functions associated with each of the six classical stress resultants, although not as additional DOFs. Some formulations include the torsion-related warping mode but reduce the number of kinematic parameters by eliminating bi-shear deformation (Gruttmann et al. 1998) and shear deformation (Rizzi & Tatone 1996, Pignataro & Ruta 2002). The co-rotational formulation of Battini & Pacoste (2002a, 2002b) allows considering or discarding shear/bi-shear deformation. Klinkel & Govindjee (2003) included three warping modes associated to the Saint-Vénant solutions for pure bending and torsion. Pimenta & Campello (2003) and Ritto-Corrêa (2004) proposed formulations that allow arbitrary cross-section deformation, although none of them has been implemented. The consideration of arbitrary cross-section deformation for initially straight geometrically exact thin-walled beams has been proposed by Gonçalves et al. (2010a, 2011).

In this paper, the geometrically exact thin-walled beam formulation proposed by Gonçalves et al. (2010a) is extended to account for initial curved geometries (not a trivial task) and some computational aspects are improved. In particular, the derivative of the torsional curvature, which is computationally expensive, is not required in the present formulation, meaning that secondary warping due to torsion constitutes an independent cross-section DOF. As in the previous formulation, arbitrary cross-section in-plane and out-of-plane deformation is allowed, even if Kirchhoff's thin plate assumption is deemed valid.

A finite element is obtained by interpolating directly the independent kinematic parameters using Hermite cubic functions and the standard isoparametric concept, meaning that the initial curved geometry of the beam is also approximated with cubic functions. The accuracy and efficiency of the proposed element are assessed through several illustrative numerical examples. For validation and comparison purposes, results obtained with refined shell finite element models are presented.

Concerning the notation, all scalar quantities, including tensor components, are represented by italic letters. Vectors, second-order tensors and matrices are identified by bold italic letters. Partial scalar derivatives are indicated by subscripts following a comma, e.g., $f_{,a} = \partial f / \partial a$, $\otimes$ is the standard tensorial product, $\times$ is the vector cross product, $\widetilde{\boldsymbol{a}}$ is the skew-symmetric second-order tensor whose axial vector is $\boldsymbol{a}$ and the standard Euclidean norm is $\|\boldsymbol{a}\| = \sqrt{\boldsymbol{a} \cdot \boldsymbol{a}}$. Finally, a virtual variation is denoted by δ and an incremental/iterative variation is preceded by Δ.

2. The thin-walled beam formulation

The proposed beam formulation relies on three fundamental assumptions:

(A1) the wall thickness is small when compared with the cross-section dimensions and is constant in each wall;

(A2) Kirchhoff's thin plate assumption holds except for torsion effects;

(A3) small strains.

With respect to an orthonormal direct reference system (X_1, X_2, X_3) with basis vectors $(\boldsymbol{E}_1, \boldsymbol{E}_2, \boldsymbol{E}_3)$, three beam configurations are defined: (i) the reference (straight) configuration, (ii) the initial (curved but undeformed) configuration and (iii) the current (deformed) configuration. The relevant vectors for a given point *B* are displayed in Fig. 1, for the reference and current configurations (the initial configuration is just a particular case of the current configuration and, therefore, is not shown in the figure).

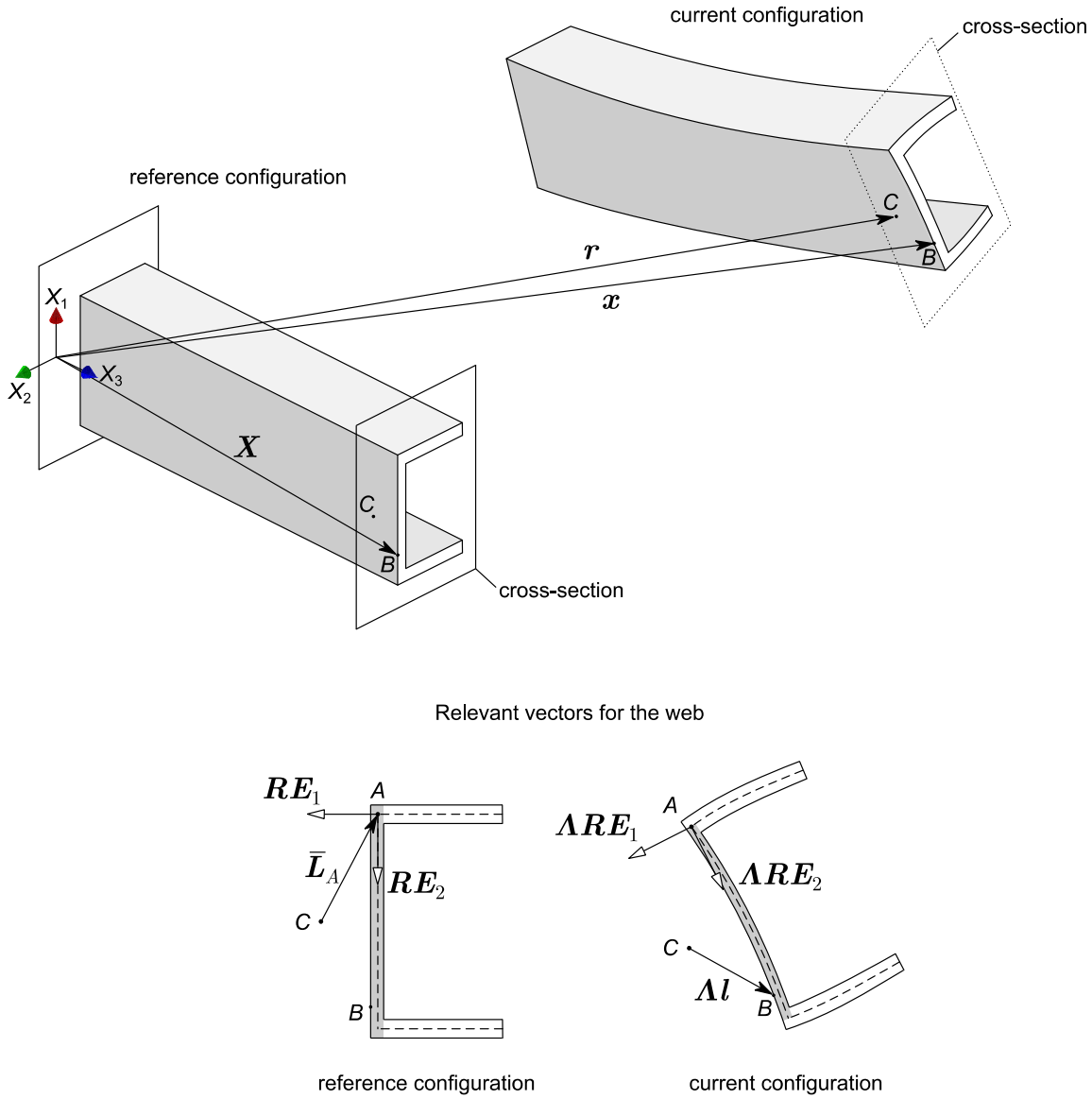

Figure 1: Reference and current configurations of a thin-walled beam.

At the reference configuration the beam is straight and mapped through

$$\boldsymbol{X} = X_3\boldsymbol{E}_3 + \bar{\boldsymbol{L}}_A + \boldsymbol{R}(X_1\boldsymbol{E}_1 + X_2\boldsymbol{E}_2), \tag{1}$$

where (i) $X_3 \in [-1;1]$, as in the usual natural coordinates concept, coinciding with the beam longitudinal axis, whose intersection with each cross-section defines the arbitrary cross-section center *C*, (ii) $\bar{\boldsymbol{L}}_A$ is a cross-section vector which references the origin *A* of each wall mid-line and $\boldsymbol{R}$ is the rotation tensor that rotates the base vectors about *A*, along X_3, such that $\boldsymbol{R}\boldsymbol{E}_1$ and $\boldsymbol{R}\boldsymbol{E}_2$ define the through-thickness and wall mid-line directions, respectively.

The initial configuration is defined by

$$\begin{aligned} &\boldsymbol{x}_0 = \boldsymbol{r}_0 + \boldsymbol{\Lambda}_0\boldsymbol{l}_0, \\ &\boldsymbol{l}_0 = \bar{\boldsymbol{L}}_A + \boldsymbol{R}\left(X_1\boldsymbol{E}_1 + X_2\boldsymbol{E}_2 + \sum_{i=1}^{D} p_0^{(i)}\boldsymbol{\chi}^{(i)}\right), \end{aligned} \tag{2}$$

where $\boldsymbol{r}_0 = \boldsymbol{r}_0(X_3)$ defines the position of the cross-section center *C*, $\boldsymbol{\Lambda}_0 = \boldsymbol{\Lambda}_0(X_3)$ is the cross-section rotation tensor, $\boldsymbol{\chi}^{(i)} = \boldsymbol{\chi}^{(i)}(X_1, X_2)$ are arbitrary cross-section deformation modes, whose scalar weight functions $p_0^{(i)} = p_0^{(i)}(X_3)$ define their amplitudes along the beam axis, and *D* is the number of deformation modes. It is important to note that the deformation modes co-rotate with the cross-section (through the rotation tensor $\boldsymbol{\Lambda}_0$), which means that their ability to describe the cross-section configuration is not affected by a finite rotation of the section.

Finally, the current configuration is given by

$$\begin{aligned} &\boldsymbol{x} = \boldsymbol{r}_0 + \hat{\boldsymbol{u}} + \hat{\boldsymbol{\Lambda}}\boldsymbol{\Lambda}_0\boldsymbol{l}, \\ &\boldsymbol{l} = \bar{\boldsymbol{L}}_A + \boldsymbol{R}\left(X_1\boldsymbol{E}_1 + X_2\boldsymbol{E}_2 + \sum_{i=1}^{D}(p_0^{(i)} + \hat{p}^{(i)})\boldsymbol{\chi}^{(i)}\right) = \boldsymbol{l}_0 + \boldsymbol{R}\sum_{i=1}^{D}\hat{p}^{(i)}\boldsymbol{\chi}^{(i)}, \end{aligned} \tag{3}$$

where the hat (^) identifies parameters that characterize the kinematics between the initial and current configurations and $\boldsymbol{\Lambda} = \hat{\boldsymbol{\Lambda}}\boldsymbol{\Lambda}_0$ is the cross-section rotation tensor between the reference and current configurations.

Due to assumptions A1 and A2, the deformation mode functions can be expressed as

$$\boldsymbol{\chi}^{(i)}(X_1, X_2) = \bar{\boldsymbol{\chi}}^{(i)}(X_2) + X_1\left(\psi_2^{(i)}(X_2)\boldsymbol{E}_2 + \psi_3^{(i)}(X_2)\boldsymbol{E}_3\right), \tag{4}$$

where $\bar{\boldsymbol{\chi}}^{(i)}$ accounts for membrane-type displacements and $X_1\psi_i$ allows for a linear through-thickness variation of the displacements, along the wall mid-line ($\psi_2^{(i)}$) and warping ($\psi_3^{(i)}$) directions. This format makes it possible to write, for the current configuration (the initial configuration is just a particular case),

$$
\begin{aligned}
&\boldsymbol{x} = \overline{\boldsymbol{x}} + X_1 \widehat{\boldsymbol{\Lambda}} \boldsymbol{\Lambda}_0 \boldsymbol{R} \left(\boldsymbol{E}_1 + \sum_{i=1}^{D} \left(\psi_2^{(i)} \boldsymbol{E}_2 + \psi_3^{(i)} \boldsymbol{E}_3 \right) \right), \\
&\overline{\boldsymbol{x}} = \boldsymbol{r}_0 + \widehat{\boldsymbol{u}} + \widehat{\boldsymbol{\Lambda}} \boldsymbol{\Lambda}_0 \bar{\boldsymbol{l}}, \\
&\bar{\boldsymbol{l}} = \bar{\boldsymbol{L}}_A + \boldsymbol{R} \left(X_2 \boldsymbol{E}_2 + \sum_{i=1}^{D} (p_0^{(i)} + \hat{p}^{(i)}) \overline{\boldsymbol{\chi}}^{(i)} \right).
\end{aligned}
\tag{5}
$$

The Green-Lagrange strains, which ensure capturing Wagner effects, are given by

$$
\widehat{\boldsymbol{E}} = \frac{1}{2} \left(\widehat{\boldsymbol{F}}^T \widehat{\boldsymbol{F}} - \boldsymbol{1} \right) = \frac{1}{2} \left((\boldsymbol{F} \boldsymbol{F}_0^{-1})^T \boldsymbol{F} \boldsymbol{F}_0^{-1} - \boldsymbol{1} \right) = \frac{1}{2} \left(\boldsymbol{F}_0^{-T} \boldsymbol{F}^T \boldsymbol{F} \boldsymbol{F}_0^{-1} - \boldsymbol{1} \right),
\tag{6}
$$

where the following deformation gradients are defined

$$
\boldsymbol{F} = \frac{d\boldsymbol{x}}{d\boldsymbol{X}}, \qquad \boldsymbol{F}_0 = \frac{d\boldsymbol{x}_0}{d\boldsymbol{X}}, \qquad \widehat{\boldsymbol{F}} = \frac{d\boldsymbol{x}}{d\boldsymbol{x}_0} = \boldsymbol{F} \boldsymbol{F}_0^{-1}.
\tag{7}
$$

For the membrane terms, to keep track of the physical meaning of each strain component, the membrane deformation tensor is back-rotated to the reference configuration through

$$
\boldsymbol{E}^M = \breve{\boldsymbol{\Lambda}}_0^T \, \widehat{\boldsymbol{E}}^M \, \breve{\boldsymbol{\Lambda}}_0,
\tag{8}
$$

where $\breve{\boldsymbol{\Lambda}}_0$ is a rotation tensor, calculated at each integration point, from the reference to the initial configuration, such that $\breve{\boldsymbol{\Lambda}}_0 \boldsymbol{E}_1$ defines the through-thickness direction (perpendicular to the wall mid-surface). If the initial configuration is free from shear and cross-section deformation, one has $\breve{\boldsymbol{\Lambda}}_0 = \boldsymbol{\Lambda}_0 \boldsymbol{R}$. This leads to the membrane deformation tensor

$$
\begin{aligned}
\boldsymbol{E}^M &= \breve{\boldsymbol{\Lambda}}_0^T \, \widehat{\boldsymbol{E}}^M \breve{\boldsymbol{\Lambda}}_0 = \frac{1}{2} \left(\breve{\boldsymbol{\Lambda}}_0^T \boldsymbol{F}_0^{-T} \boldsymbol{F}^T \boldsymbol{F} \boldsymbol{F}_0^{-1} \breve{\boldsymbol{\Lambda}}_0 - \boldsymbol{1} \right) \\
&= \frac{1}{2} \left(\breve{\boldsymbol{\Lambda}}_0^T \boldsymbol{\Lambda}_0 \boldsymbol{R} \boldsymbol{G}_0^{-T} \boldsymbol{G}^T \boldsymbol{G} \boldsymbol{G}_0^{-1} (\boldsymbol{\Lambda}_0 \boldsymbol{R})^T \breve{\boldsymbol{\Lambda}}_0 - \boldsymbol{1} \right),
\end{aligned}
\tag{9}
$$

where the following relations were employed

$$
\begin{aligned}
&\boldsymbol{F} = \widehat{\boldsymbol{\Lambda}} \boldsymbol{\Lambda}_0 \boldsymbol{R} \sum_{i=1}^{3} (\boldsymbol{g}_i \otimes \boldsymbol{E}_i) = \widehat{\boldsymbol{\Lambda}} \boldsymbol{\Lambda}_0 \boldsymbol{R} \boldsymbol{G}, \\
&\boldsymbol{F}_0 = \boldsymbol{\Lambda}_0 \boldsymbol{R} \sum_{i=1}^{3} (\boldsymbol{g}_{0i} \otimes \boldsymbol{E}_i) = \boldsymbol{\Lambda}_0 \boldsymbol{R} \boldsymbol{G}_0,
\end{aligned}
\tag{10}
$$

with

$$
\begin{aligned}
&\boldsymbol{g}_2 = \boldsymbol{E}_2 + \sum_{i=1}^{D} (p_0^{(i)} + \hat{p}^{(i)}) \overline{\boldsymbol{\chi}}_{,2}^{(i)}, \\
&\boldsymbol{g}_3 = \boldsymbol{E}_3 + \boldsymbol{\Gamma} + \boldsymbol{K} \times \left(\boldsymbol{R}^T \bar{\boldsymbol{l}} \right) + \sum_{i=1}^{D} (p_{0,3}^{(i)} + \hat{p}_{,3}^{(i)}) \overline{\boldsymbol{\chi}}^{(i)}, \\
&\boldsymbol{\Gamma} = (\boldsymbol{\Lambda} \boldsymbol{R})^T \left(\boldsymbol{r}_{0,3} + \widehat{\boldsymbol{u}}_{,3} \right) - \boldsymbol{E}_3, \\
&\boldsymbol{K} = \mathrm{axi} \left((\boldsymbol{\Lambda} \boldsymbol{R})^T \boldsymbol{\Lambda}_{,3} \boldsymbol{R} \right).
\end{aligned}
\tag{11}
$$

Furthermore, due to Kirchhoff's assumption,

$$\|\boldsymbol{g}_1\| = 1, \quad \boldsymbol{g}_1 \cdot \boldsymbol{g}_2 = \boldsymbol{g}_1 \cdot \boldsymbol{g}_3 = 0 \tag{12}$$

and, naturally, $\boldsymbol{g}_1$ does not affect the membrane strains. It should be noted that the strain measures $\boldsymbol{\Gamma}$ and $\boldsymbol{K}$ quantify the beam axis shear/extension and curvature, respectively (Simo, 1985).

Since the strains are assumed small (assumption A3), the bending terms can be uncoupled from the membrane ones and it suffices to subtract the co-rotational (bending) strains between the reference/current and reference/initial configurations. Furthermore, according to assumption A2, Kirchhoff's thin-plate assumption is adopted for all deformation modes except the torsion-related secondary warping mode (this mode is identified by $i = 1$ and is designated by $\hat{p}_t\psi_{t3}$). This approach differs from that proposed by Gonçalves et al. (2010a), since it uncouples $\hat{p}_t$ and the torsional component of the curvature $\widehat{K}_3 = K_3 - K_{30}$, thus avoiding the computation of the derivative of this component and its virtual and incremental/iterative variations, which are computationally expensive. With these assumptions, the bending strains are given by

$$\begin{aligned}
E_{22}^B &= -X_1 \sum_{i=1}^{D} \hat{p}^{(i)} \bar{\chi}_{1,22}^{(i)}, \\
E_{33}^B &= -X_1 \left(K_2 - K_{20} - \hat{p}_{t,3}\psi_{t3} + \sum_{i=2}^{D} \hat{p}_{,33}^{(i)} \bar{\chi}_1^{(i)} \right), \\
2E_{13}^B &= (\hat{p}_t - K_3 + K_{30})\psi_{t3}, \\
2E_{23}^B &= X_1 \left(K_3 - K_{30} + \hat{p}_t - 2\sum_{i=2}^{D} \hat{p}_{,3}^{(i)} \bar{\chi}_{1,2}^{(i)} \right).
\end{aligned} \tag{13}$$

Note that, if null bi-shear due to secondary warping is enforced, as in Gonçalves et al. (2010a), then $\hat{p}_t = \widehat{K}_3 = K_3 - K_{30}$, leading to $E_{13}^B = 0$ but, on the other hand, the longitudinal strains E_{33}^B become dependent on $\widehat{K}_{3,3}$, as mentioned above.

The equilibrium equations are obtained from the virtual work principle, written at the reference configuration. Using Voigt notation and assuming, for simplicity, that a single concentrated force $\boldsymbol{Q}$ is applied at a point of the wall mid-surface, one has

$$\delta W = \delta W_{int} + \delta W_{ext} = 0 \Leftrightarrow -\int_V \delta \boldsymbol{E}^T \boldsymbol{S}\, J_0 dV + \delta \bar{\boldsymbol{x}}^T \boldsymbol{Q} = 0, \tag{14}$$

where V is the beam volume at the reference configuration, $J_0 = \det(\boldsymbol{F}_0)$ and $\boldsymbol{S}$ are back-rotated second Piola-Kirchhoff stresses.

Before writing the virtual variation of the strain components, it is necessary to establish a proper parametrization of the rotation tensor. In this work the rotation vector $\boldsymbol{\theta} = \boldsymbol{\theta}(X_3)$ is employed, which is related to the rotation tensor through the well-known Rodrigues formula (see, e.g., Goldstein, 1980)

$$\boldsymbol{\Lambda} = \mathbf{1} + a_1\widetilde{\boldsymbol{\theta}} + a_2\widetilde{\boldsymbol{\theta}}^2, \tag{15}$$

with the following family of auxiliary functions defined by Ritto-Corrêa & Camotim (2002)

$$\begin{aligned} &a_1 = \frac{\sin\theta}{\theta}, a_2 = \frac{1-\cos\theta}{\theta^2}, a_3 = \frac{\theta-\sin\theta}{\theta^3}, \\ &b_1 = \frac{\theta\cos\theta-\sin\theta}{\theta^3}, b_2 = \frac{\theta\sin\theta-2+2\cos\theta}{\theta^4}, b_3 = \frac{-2\theta+3\sin\theta-\theta\cos\theta}{\theta^5}, \end{aligned} \tag{16}$$

where $\theta = \|\boldsymbol{\theta}\|$.

The independent kinematic parameters defining the current configuration are grouped in vector $\widehat{\boldsymbol{\phi}}$, as follows

$$\left[\widehat{\boldsymbol{\phi}}\right]^T = \left[\widehat{\boldsymbol{u}}^T \;\; \widehat{\boldsymbol{\theta}}^T \;\; \hat{p}^{(1)} \;\; \cdots \;\; \hat{p}^{(D)}\right], \tag{17}$$

where $\hat{p}^{(1)} = \hat{p}_t$. The initial configuration is defined analogously, using the subscript "0", i.e.,

$$\left[\widehat{\boldsymbol{\phi}}_0\right]^T = \left[\boldsymbol{u}_0^T \;\; \widehat{\boldsymbol{\theta}}_0^T \;\; p_0^{(1)} \;\; \cdots \;\; p_0^{(D)}\right]. \tag{18}$$

For the calculation of the virtual work, the following expressions of the virtual variations are required

$$\delta\boldsymbol{g}_2 = \sum_{i=1}^{D} \delta\hat{p}^{(i)}\overline{\boldsymbol{\chi}}_{,2}^{(i)}, \tag{19}$$

$$\delta\boldsymbol{g}_3 = \delta\boldsymbol{\Gamma} + \delta\boldsymbol{K}\times\left(\boldsymbol{R}^T\bar{\boldsymbol{l}}\right) + \boldsymbol{K}\times\left(\boldsymbol{R}^T\delta\bar{\boldsymbol{l}}\right) + \sum_{i=1}^{D}\delta\hat{p}_{,3}^{(i)}\overline{\boldsymbol{\chi}}^{(i)}, \tag{20}$$

$$\delta\bar{\boldsymbol{l}} = \boldsymbol{R}\sum_{i=1}^{D}\delta\hat{p}^{(i)}\overline{\boldsymbol{\chi}}^{(i)}, \tag{21}$$

$$\delta\boldsymbol{\Gamma} = \boldsymbol{R}^T\,\boldsymbol{\Xi}_{D\widehat{\boldsymbol{\Lambda}}^T}\left(\boldsymbol{r}_{0,3}+\widehat{\boldsymbol{u}}_{,3}\right)\delta\widehat{\boldsymbol{\theta}} + (\boldsymbol{\Lambda}\boldsymbol{R})^T\delta\widehat{\boldsymbol{u}}_{,3}, \tag{22}$$

$$\delta\boldsymbol{K} = \boldsymbol{R}^T\,\boldsymbol{\Xi}_{D\boldsymbol{T}^T}\left(\boldsymbol{\theta}_{,3}\right)\delta\widehat{\boldsymbol{\theta}} + \boldsymbol{R}^T\boldsymbol{T}^T\delta\widehat{\boldsymbol{\theta}}_{,3}, \tag{23}$$

$$\delta E_{22}^B = -X_1\sum_{i=1}^{D}\delta\hat{p}^{(i)}\bar{\chi}_{1,22}^{(i)}, \tag{24}$$

$$\delta E_{33}^B = -X_1\left(\delta K_2 - \delta\hat{p}_{t,3}\psi_{t3} + \sum_{i=2}^{D}\delta\hat{p}_{,33}^{(i)}\bar{\chi}_1^{(i)}\right), \tag{25}$$

$$2\delta E_{13}^B = (\delta\hat{p}_t - \delta K_3)\psi_{t3}, \tag{26}$$

$$2\delta E_{23}^B = X_1\left(\delta K_3 + \delta\hat{p}_t - 2\sum_{i=2}^{D}\delta\hat{p}_{,3}^{(i)}\bar{\chi}_{1,2}^{(i)}\right), \tag{27}$$

$$\delta\overline{\boldsymbol{x}} = \delta\widehat{\boldsymbol{u}} + \boldsymbol{\Xi}_{D\widehat{\boldsymbol{\Lambda}}}\left(\boldsymbol{\Lambda}_0\bar{\boldsymbol{l}}\right)\delta\widehat{\boldsymbol{\theta}} + \widehat{\boldsymbol{\Lambda}}\boldsymbol{\Lambda}_0\boldsymbol{R}\sum_{i=1}^{D}\delta\hat{p}^{(i)}\overline{\boldsymbol{\chi}}^{(i)}. \tag{28}$$

These variations can be written in terms of the independent kinematic parameters using the auxiliary operators originally defined by Ritto-Corrêa & Camotim (2002), given by

$$\begin{aligned}
&\boldsymbol{\Xi}_{D\boldsymbol{\Lambda}}(\boldsymbol{a}) = -a_1\widetilde{\boldsymbol{a}} - a_2\left(\widetilde{\widetilde{\boldsymbol{\theta}}\boldsymbol{a}} + \widetilde{\boldsymbol{\theta}}\widetilde{\boldsymbol{a}}\right) + b_1\left(\widetilde{\boldsymbol{\theta}}\boldsymbol{a}\otimes\boldsymbol{\theta}\right) + b_2\left(\widetilde{\boldsymbol{\theta}}^2\boldsymbol{a}\otimes\boldsymbol{\theta}\right),\\
&\boldsymbol{\Xi}_{D\boldsymbol{\Lambda}^T}(\boldsymbol{a}) = a_1\widetilde{\boldsymbol{a}} - a_2\left(\widetilde{\widetilde{\boldsymbol{\theta}}\boldsymbol{a}} + \widetilde{\boldsymbol{\theta}}\widetilde{\boldsymbol{a}}\right) - b_1\left(\widetilde{\boldsymbol{\theta}}\boldsymbol{a}\otimes\boldsymbol{\theta}\right) + b_2\left(\widetilde{\boldsymbol{\theta}}^2\boldsymbol{a}\otimes\boldsymbol{\theta}\right),\\
&\boldsymbol{\Xi}_{D\boldsymbol{T}^T}(\boldsymbol{a}) = a_2\widetilde{\boldsymbol{a}} - a_3\left(\widetilde{\widetilde{\boldsymbol{\theta}}\boldsymbol{a}} + \widetilde{\boldsymbol{\theta}}\widetilde{\boldsymbol{a}}\right) - b_2\left(\widetilde{\boldsymbol{\theta}}\boldsymbol{a}\otimes\boldsymbol{\theta}\right) + b_3\left(\widetilde{\boldsymbol{\theta}}^2\boldsymbol{a}\otimes\boldsymbol{\theta}\right),\\
&\boldsymbol{T}^T = \mathbf{1} - a_2\widetilde{\boldsymbol{\theta}} + a_3\widetilde{\boldsymbol{\theta}}^2.
\end{aligned} \tag{29}$$

The incremental/iterative linearization of the virtual work equation (14), required to obtain the tangent stiffness matrix, is given by

$$\Delta\delta W = -\int_V (\Delta\delta\boldsymbol{E}^T\boldsymbol{S} + \delta\boldsymbol{E}^T\boldsymbol{C}_t\,\Delta\boldsymbol{E})J_0 dV + \Delta\delta\overline{\boldsymbol{x}}^T\boldsymbol{Q}, \tag{30}$$

where $\boldsymbol{C}_t$ is a tangent plane stress constitutive matrix for the particular material adopted, extended to include through-thickness shearing. For a St. Vénant-Kirchhoff material law (adopted in all the examples presented in Section 3), the relevant stress and strain vectors are $\boldsymbol{S}^T = [S_{22}\ \ S_{33}\ \ S_{23}\ \ S_{13}]$ and $\boldsymbol{E}^T = [E_{22}\ \ E_{33}\ \ 2E_{23}\ \ 2E_{13}]$, leading to

$$\boldsymbol{C}_t = \boldsymbol{C} = \begin{bmatrix} \dfrac{E}{1-\nu^2} & \dfrac{\nu E}{1-\nu^2} & 0 & 0 \\ \dfrac{\nu E}{1-\nu^2} & \dfrac{E}{1-\nu^2} & 0 & 0 \\ 0 & 0 & G & 0 \\ 0 & 0 & 0 & G \end{bmatrix}, \tag{31}$$

where E is Young's modulus, G is the shear modulus and ν is Poisson's ratio.

The linearization of the virtual work equation (30) can also be written in terms of the independent kinematic parameters using the auxiliary operators introduced by Ritto-Corrêa & Camotim (2002) and further developed by Gonçalves et al. (2010a). However, the expressions are rather lengthy and therefore are not presented in this paper.

The beam finite element is obtained by interpolating all the kinematic parameters in $\widehat{\boldsymbol{\phi}}$ and $\boldsymbol{\phi}_0$ using Hermite cubic functions. This leads to a two-node element with $2(6+D)$ DOFs per node, where D is the number of deformation modes included in the analysis. The first two modes are always associated with torsion-related warping, namely secondary ($i = 1$) and primary warping ($i = 2$). The integrations are carried out with Gauss quadrature, using 3×3 points along X_3 and X_2, respectively, in each wall. This corresponds to reduced integration along the length (X_3) and transverse (X_2) directions, to mitigate shear and membrane locking. Along X_1 the integration is analytical. The finite element procedure was implemented in MATLAB (2010), including a post-processing module to visualize the beam configuration.

3. Numerical examples

All examples presented in this Section concern 90° circular I-section cantilever arches. Although the present formulation can handle other initial configurations, this one was chosen since it is

significantly easier to model with shell elements (which are used for validation and comparison purposes). The built-in end prevents all displacements and rotations, including warping. With the proposed element, this boundary condition is enforced by setting

$$\widehat{\boldsymbol{u}}(0) = \widehat{\boldsymbol{\theta}}(0) = \hat{p}^{(i)} = 0, \tag{32}$$

$$\hat{p}_{,3}^{(i)}(0) = 0, \tag{33}$$

where Eq. (33) applies only to the modes involving transverse bending, due to Kirchhoff's assumption (e.g., it does not apply to the torsion-related secondary and primary warping modes).

The GBT cross-section deformation modes are obtained using GBTUL 2.06 (Gonçalves et al. 2010b, 2014; Bebiano et al. 2015, 2018), a freeware program which can be downloaded from http://www.civil.ist.utl.pt/gbt/. However, GBTUL generates linear transverse extension modes (along X_2 in each wall) and cubic modes along X_1, causing a severe mismatch of the polynomial degree of the deformation mode functions which leads to over-stiff solutions in geometrically non-linear problems. This issue is avoided by introducing quadratic transverse extension modes in each wall (Gonçalves & Camotim 2012, Martins et al. 2018).

In all examples, the results obtained with the proposed element are compared with refined four-node MITC (Mixed Interpolation of Tensorial Components) shell finite element models, analyzed using ADINA (Bathe 2019).

3.1 Large displacement analysis

The first example consists of the 6 m long 90º circular arch displayed in Fig. 2, which is loaded by an out-of-plane force applied at the centroid of the free end cross-section, causing coupled flexural-torsional phenomena (Gonçalves, 2019). This cross-section is quite compact, meaning that cross-section deformation plays a negligible role. Therefore, this example aims at showing that the proposed element handles complex problems involving finite torsional/bending rotations.

The graph in Fig. 2 displays the load-displacement plot obtained (i) with the shell model shown in the bottom right of the figure, (ii) six two-node (straight) geometrically exact elements with torsion-related warping (Gonçalves 2019) and (iii) the proposed curved formulation, using 6 or 50 elements and including only the torsion-related warping deformation modes. It is observed that the predictive capacity of the proposed element is much higher than that of the two-node (straight) beam element. In fact, with the proposed formulation, the results obtained with only 6 elements already match very accurately the shell model load-displacement curve up to very large displacements. Using 50 elements does not improve the results significantly.

The deformed configurations shown in the bottom of Fig. 2 concern a lateral displacement equal to 3 m and were obtained with the proposed beam model (6 elements rendered with four subdivisions in each wall — four flanges and one web — and along the length) and the shell model. An excellent match is observed, even though the beam undergoes severe bending-torsion phenomena with large displacements and finite rotations.

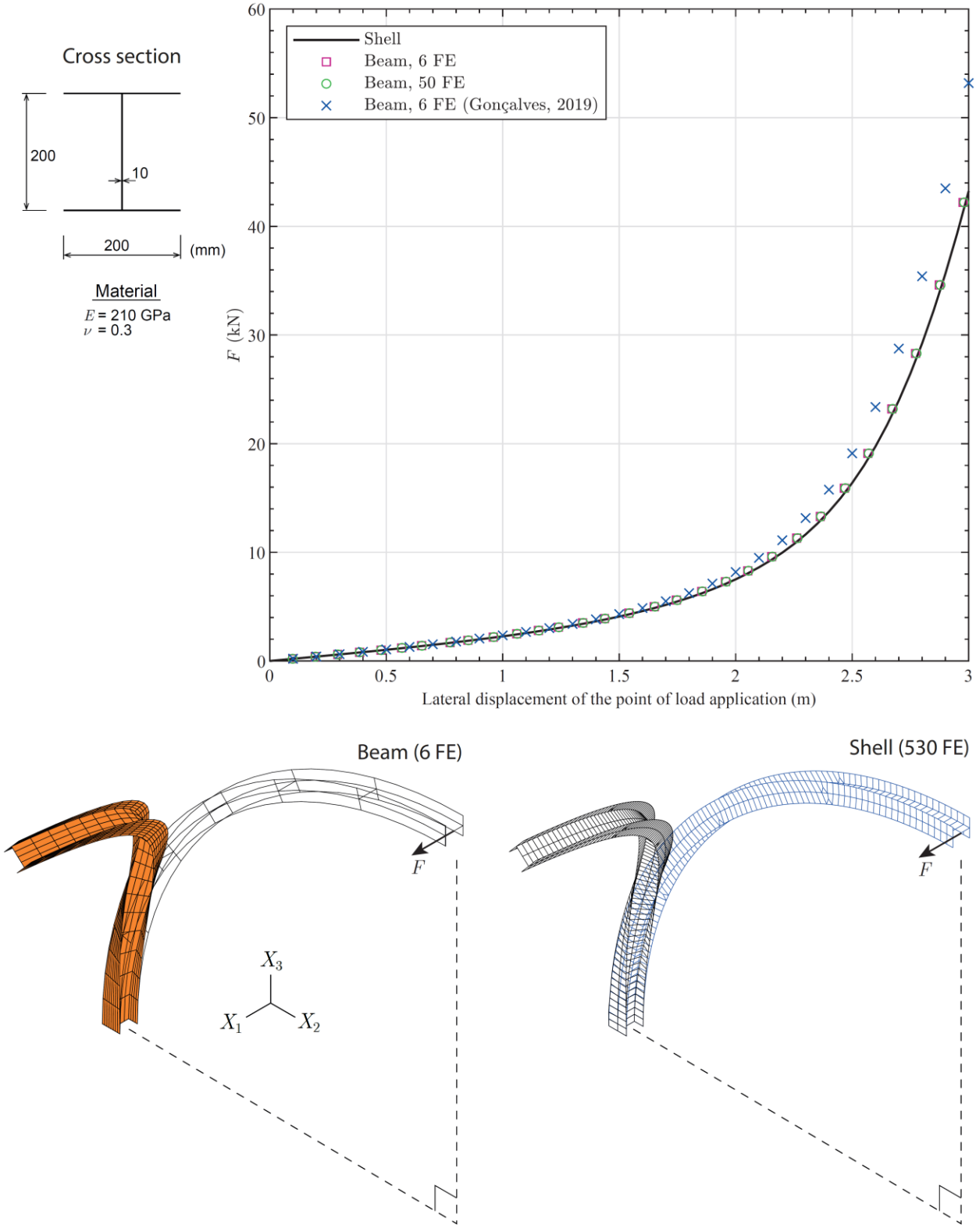

Figure 2: 90º circular arch with compact cross-section, subjected to bending-torsion.

In the next examples, a slender wide-flange cross-section is selected (see Fig. 3), to trigger local deformation. The cross-section discretization employed to obtain the GBT deformation modes is displayed at the top of the figure and involves one intermediate node in each wall. Using GBTUL, this leads to 33 deformation modes, although those involving cross-section rigid-body motions (six modes) must not be included in the present formulation, to avoid linear dependency on $\widehat{\boldsymbol{u}}$ and $\widehat{\boldsymbol{\theta}}$ — for simplicity, the mode numbering in the figure corresponds to that obtained with GBTUL. Recall that, besides the modes shown in the figure, quadratic transverse extension modes in each wall (10 modes) and the torsion-related secondary warping mode are also included in the proposed formulation, leading to a total of 38 deformation modes.

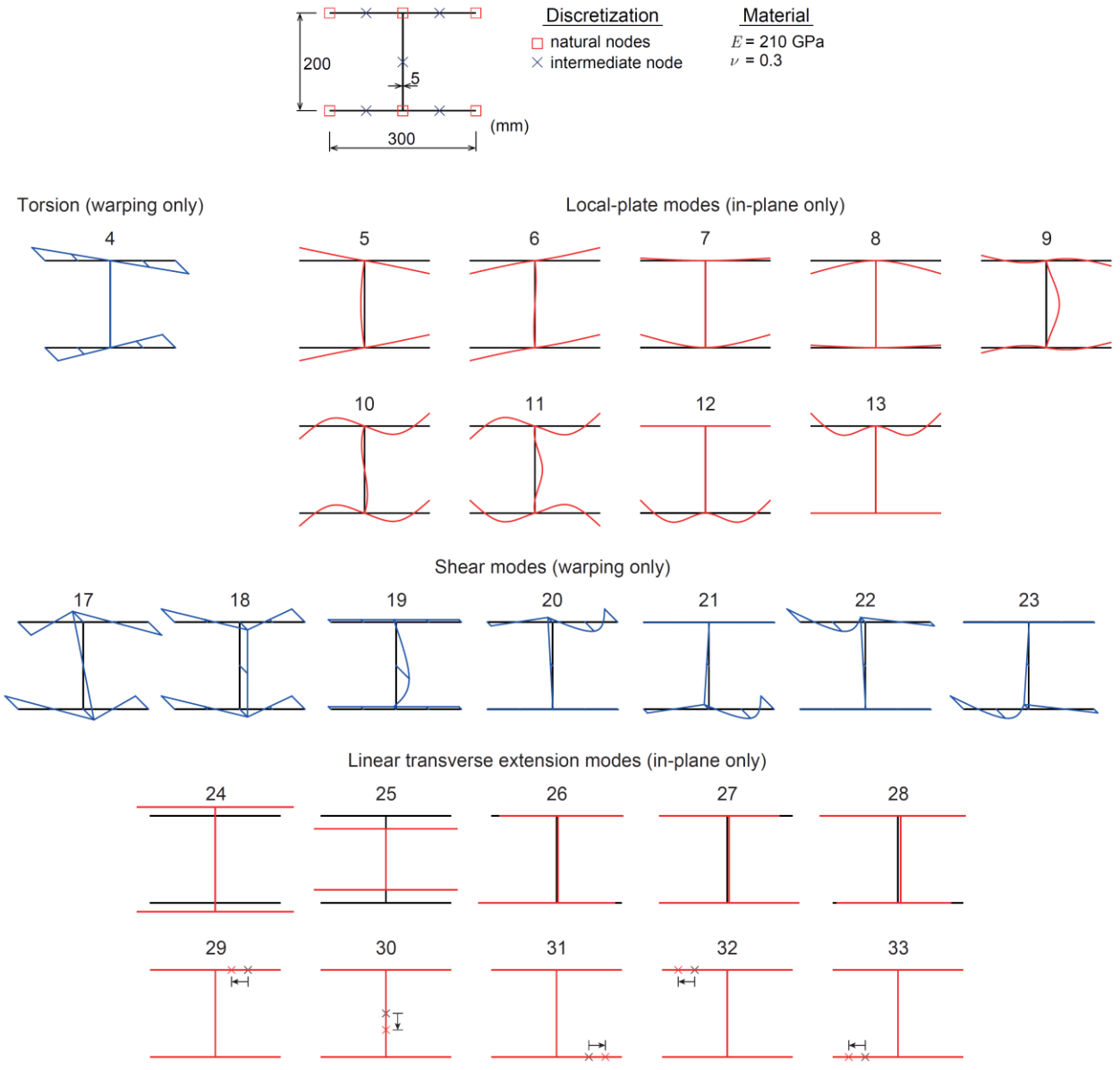

Figure 3: Most relevant deformation cross-section modes for the slender cross-section.

Again, a 6 m long 90º circular I-section arch is analyzed, but the lateral force is now applied at the flange free end, which is quite challenging to model with the proposed formulation — the load eccentricity is accounted for in the geometric term $\Delta\delta\bar{\boldsymbol{x}}^T$ in Eq. (30), which is far from trivial when considering finite rotations combined with cross-section deformation.

The results are displayed in Fig. 4. The graph plots the evolution of the lateral displacement of the point of load application, obtained with (i) the shell model displayed in the bottom right of the figure and (ii) the proposed element, using either 20 or 50 equal length elements and several sets of deformation modes. These results prompt the following remarks:

(i) The proposed formulation with only the torsion-related warping modes departs from the shell element results for loads above 1 kN. This demonstrates that cross-section deformation plays a significant role starting at this load level.

(ii) It is concluded that the present model can capture almost exactly the shell model results by considering 50 elements and all deformation modes. Considering either less deformation modes (in particular, only the torsion-related and the local-plate modes) and/or finite elements does not lead to accurate results.

(iii) The deformed configurations shown in the bottom of the figure concern the maximum displacement plotted in the graph in Fig. 4 (approximately 1.8 m) and provide further evidence of the excellent match obtained between the proposed element and the shell model. Note that local buckling near the support is observed in both models and that, due to the complex torsion-bending deformation, the point of load application does not undergo the highest lateral displacement.

Next, the beam length is reduced to π (the axis radius equals 2.0 m), in order to trigger more severe local deformation. The corresponding results are shown in Fig. 5. Once again, the graph displays the evolution of the point of load application, obtained with (i) the shell model shown in the bottom-right of the figure and (ii) the proposed element, using either 20 or 40 equal length elements and several sets of deformation modes. These results lead to the following conclusions:

(i) The shell deformed configuration displayed in the bottom right of the figure clearly shows that cross-section deformation occurs not only at the free end section (where the load is applied), but also near the support, as well as torsion-bending.

(ii) The proposed formulation with only the torsion-related warping modes fails to capture the shell model results, even for very low loads. However, excellent results are obtained if 40 elements are considered and all deformation modes are included in the analysis. As in the previous example, considering either less deformation modes (only the torsion-related and the local-plate modes) and/or finite elements leads to inaccurate results.

(iii) The deformed configurations displayed in the bottom of the figure concern the maximum displacement plotted in the graph in Fig. 5 (those corresponding to the proposed formulation were obtained with all deformation modes). It is observed that the deformed configuration obtained with 20 finite elements matches rather well the shell model one, but does not capture exactly the local deformation occurring near the support. However, with 40 elements, a virtually perfect match is obtained.

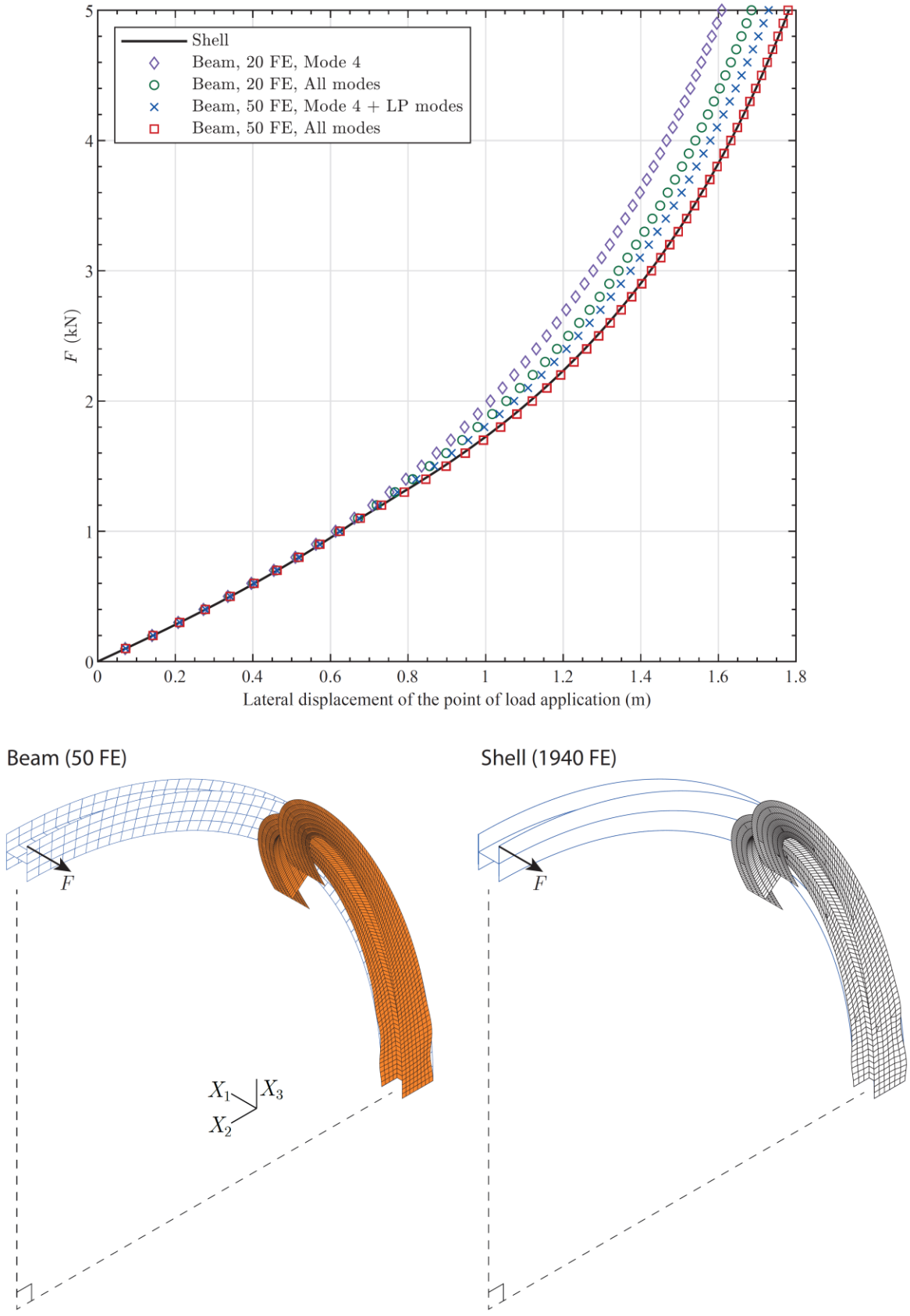

Figure 4: 90º circular arch with slender cross-section.

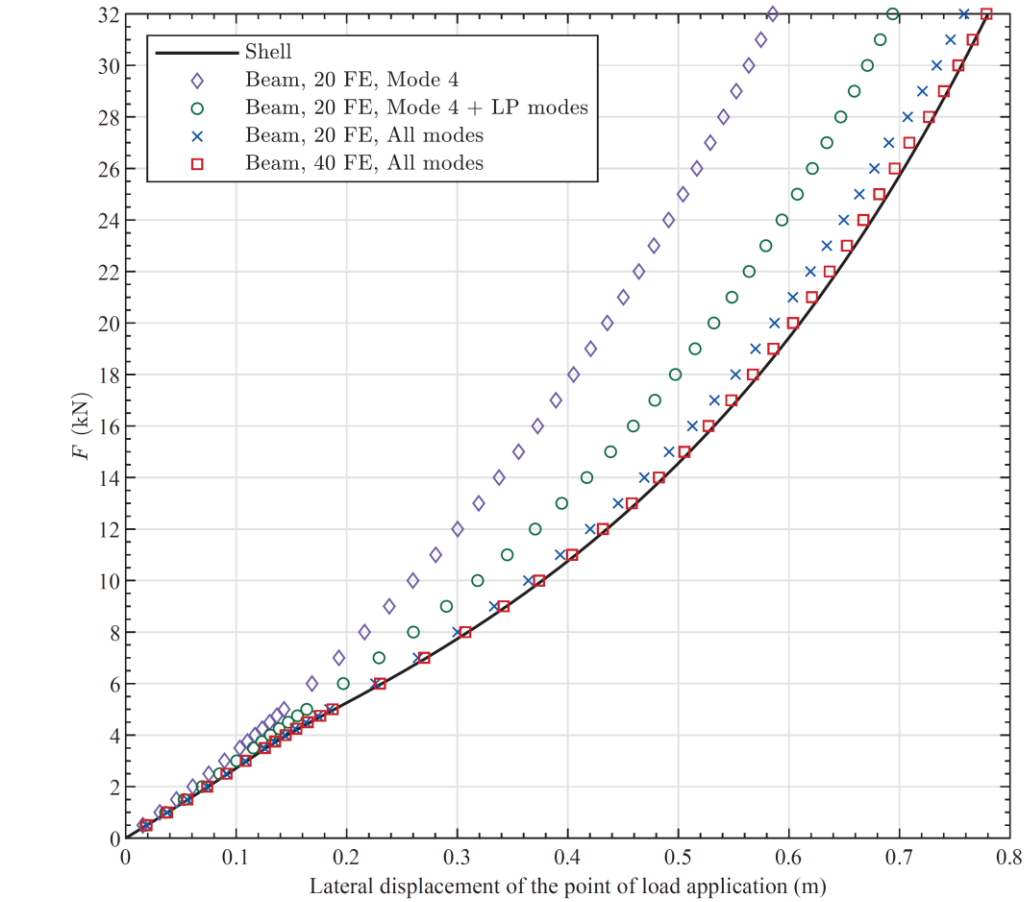

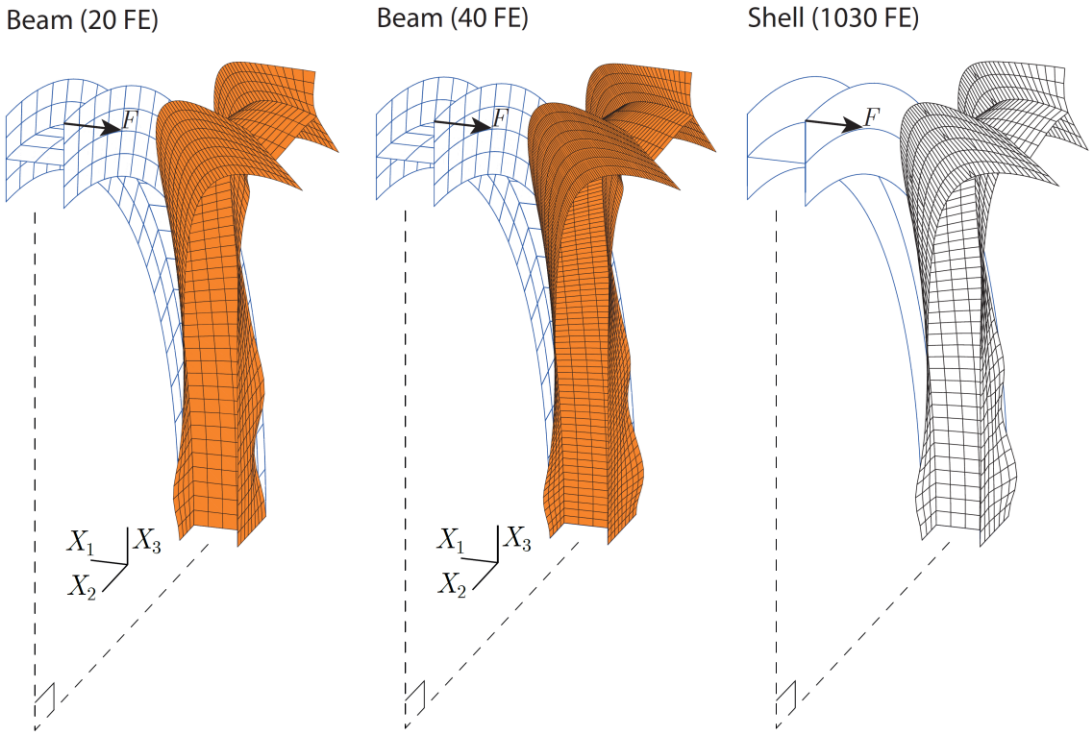

Figure 5: Short 90º circular arch with slender cross-section.

3.2 Linear Stability Analysis

Since the proposed element is geometrically exact, it can be quite easily adapted to perform linear stability analyses (LSA) and, thus, calculate bifurcation loads and the associated buckling mode shapes. It should be noted that this is a rather significant feature of the proposed formulation, since the accuracy of a LSA is highly dependent on the accuracy of the geometrically non-linear terms considered. Without a geometrically exact approach, these non-linear terms are not easily derived for initially curved members.

According to the LSA concept, the pre-buckling stresses $\boldsymbol{S}$ are first calculated on the basis of a linear analysis, which only requires the computation of the tangent stiffness matrix of the first iteration, $\boldsymbol{K}$. This matrix is obtained from the discretized form of (30), resulting in

$$\Delta\delta W(\boldsymbol{S}=\boldsymbol{0},\widehat{\boldsymbol{\phi}}=\boldsymbol{0}) = -\int_V \delta\boldsymbol{\varepsilon}^T\boldsymbol{C}_t\,\Delta\boldsymbol{\varepsilon}\,J_0 dV, \tag{34}$$

where $\boldsymbol{\varepsilon}$ is the small strain tensor. On the other hand, the geometric stiffness matrix $\boldsymbol{G}$ is obtained from the discretized form of the initial stress part of (30), which now reads

$$\Delta\delta W_{geo}(\boldsymbol{S},\widehat{\boldsymbol{\phi}}=\boldsymbol{0}) = -\lambda\int_V \Delta\delta\boldsymbol{E}^T\boldsymbol{S}\,J_0 dV + \Delta\delta\bar{\boldsymbol{x}}^T\boldsymbol{Q}, \tag{35}$$

where $\boldsymbol{E}$ is calculated for $\widehat{\boldsymbol{\phi}}=\boldsymbol{0}$ and λ is the load factor.

With the previous equations, the standard LSA eigenvalue problem emerges,

$$(\boldsymbol{K}+\lambda\boldsymbol{G})\boldsymbol{d}=\boldsymbol{0}, \tag{36}$$

where the eigenvalues λ correspond to the bifurcation loads and the corresponding eigenvectors $\boldsymbol{d}$ define the buckling modes.

Using this approach, the first two bifurcation loads and associated buckling modes are calculated for the shorter 90º circular I-section arch of Fig. 5. In this case the loading consists of a downward 1 kN vertical force, applied at the centroid of the free end cross-section, as shown in Fig. 6. This figure displays the results obtained with the proposed formulation, using all modes and 40 equal length finite elements (this number of elements was found necessary to obtain convergence of the bifurcation loads), and a shell model. Furthermore, Fig. 7 plots the mode amplitude functions, along the beam length, for both buckling modes.

The results displayed in Fig. 6 show that the bifurcation load parameters λ obtained with the proposed formulation fall within 5.0% of those provided by the shell model, and that the buckling mode shapes are in excellent agreement. These modes are characterized by local deformation near the support, with the inward (compressed) flanges exhibiting several half-waves. It should be noted that this is a quite complex problem from a numerical point of view, since the two bifurcation loads are very close.

Concerning the mode amplitude graphs in Fig. 7, it is concluded that the first buckling mode is symmetric with respect to the beam axis plane. This mode is essentially characterized by several local-plate deformation modes (mostly modes 7, 8 and 5) that exhibit four half waves whose amplitudes are higher near the support and decrease towards the free end. Mode 2 is not symmetric and is much more complex:

(i) The deformation modes exhibiting the highest participations are the local modes 6, 7 and 8. Their amplitudes are again higher near the support and "damp out" as one moves towards the free end.

(ii) Both torsion-related warping modes (primary and secondary) are now present. The amplitudes of these modes are somewhat distinct near the support (the secondary warping mode exhibits some undulation), but they virtually coincide for $X_3/L > 0.3$.

(iii) The participation of the r_1 and θ_2 parameters is also noteworthy, particularly at the free end. This shows that a horizontal displacement occurs due to bending, which is a consequence of the lack of symmetry of the buckling mode.

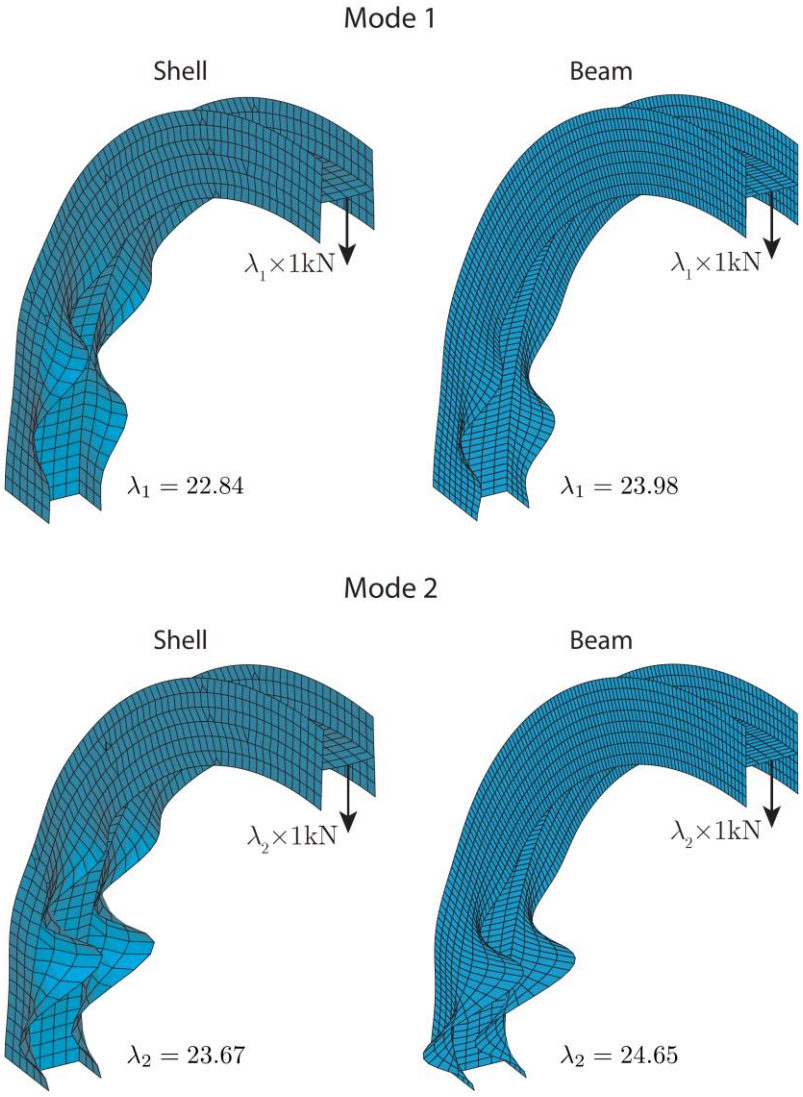

Figure 6: First two buckling modes of the short 90º circular arch.

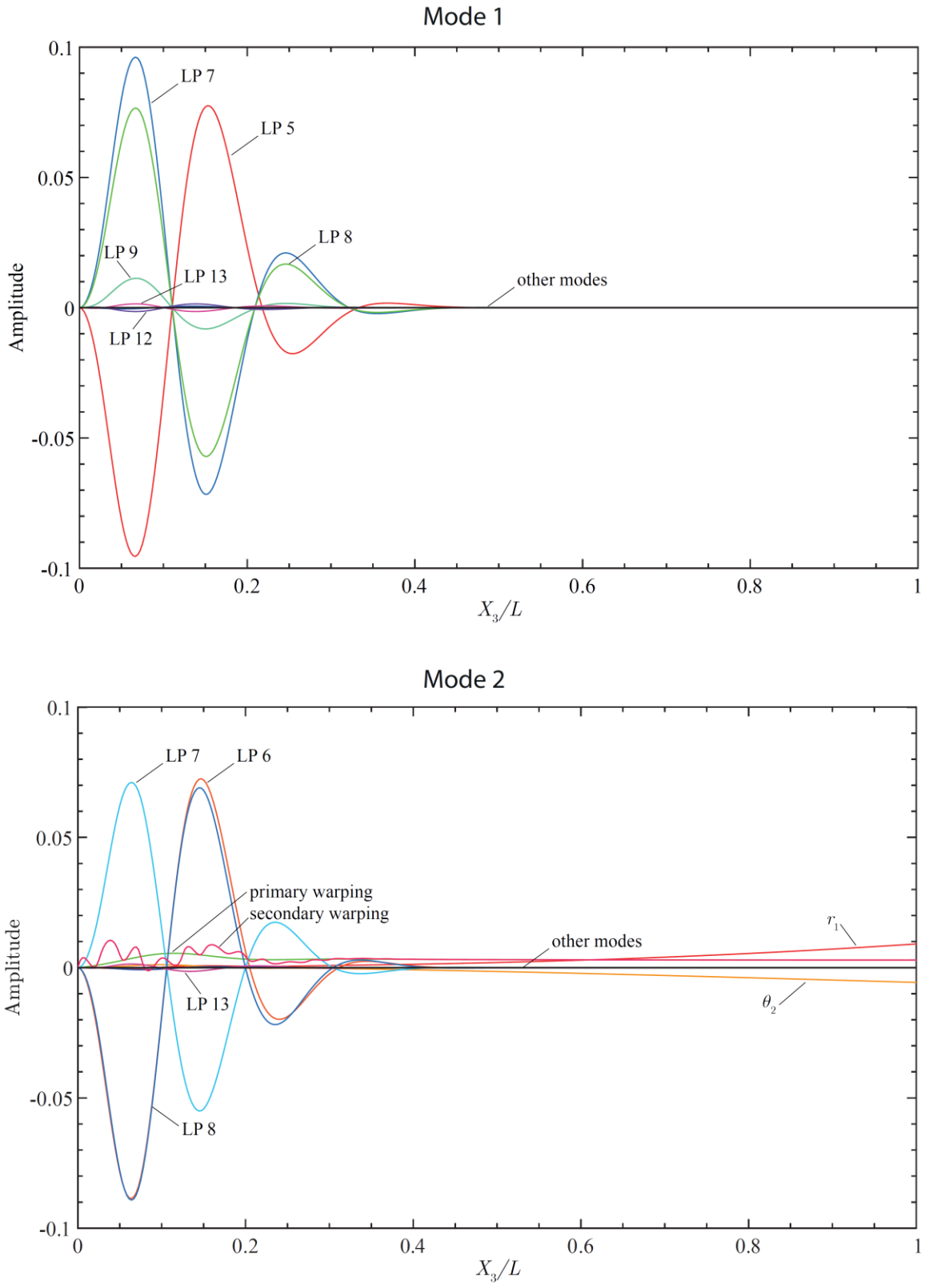

Figure 7: Deformation mode amplitude functions of the first two buckling modes of the short 90º circular arch.

4. Concluding remarks

This paper presented a new geometrically exact beam formulation that handles naturally curved thin-walled members undergoing global-local displacements. In order to describe cross-section deformation, Generalized Beam Theory deformation modes are employed, which means that Kirchhoff's thin plate assumption is adopted. However, through-thickness shearing resulting from secondary warping torsion is allowed, thus avoiding the calculation of the computationally expensive derivative of the torsional curvature (and of its virtual and incremental/iterative variations). The finite element implementation of the proposed formulation was obtained by interpolating the independent kinematic parameters using Hermite cubic polynomials, resulting in an element with $4(6 + D)$ DOFs, where D is the number of deformation modes (including torsion-related primary and secondary warping).

The accuracy and efficiency of the proposed finite element was demonstrated through several illustrative numerical examples concerning the calculation of (i) deformed configurations involving large displacements and finite rotations, combined with cross-section deformation, and (ii) bifurcation loads and associated buckling mode shapes (Linear Stability Analysis). For validation and comparison purposes, shell finite element model results were provided. It was concluded that the proposed element leads to excellent results in spite of the complexity of the problems analyzed.

Work is currently under way to include plasticity and develop a mixed finite element.

Acknowledgement

The first author gratefully acknowledges the financial support of FCT (Fundação para a Ciência e a Tecnologia, Portugal), through the doctoral scholarship SFRH/BD/120062/2016.

References

Atluri, S., Iura, M., Vasudevan, S. (2001). "A consistent theory of finite stretches and finite rotations, in space-curved beams of arbitrary cross-section." Computational Mechanics 27 (4) 271-281.

Bathe K. J. (2019). *ADINA System*, ADINA R&D Inc.

Battini, J., Pacoste, C. (2002a). "Co-rotational beam elements with warping effects in instability problems." *Computer Methods in Applied Mechanics and Engineering*, 191 1755-1789.

Battini, J., Pacoste, C. (2002b). "Plastic instability of beam structures using co-rotational elements." *Computer Methods in Applied Mechanics and Engineering*, 191 5811-5831.

Bebiano, R., Gonçalves, R., Camotim, D. (2015). "A Cross-Section Analysis Procedure to Rationalise and Automate the Performance of GBT-Based Structural Analyses." *Thin-Walled Structures* 92 29-47.

Bebiano, R., Camotim, D., Gonçalves, R. (2018). "GBTUL 2.0 – a second-generation code for the GBT-based buckling and vibration analysis of thin-walled members." *Thin-Walled Structures* 124 235-253.

Goldstein, H. (1980). *Classical Mechanics*. Addison-Wesley, Reading, Massachusetts, USA.

Gonçalves, R., Ritto-Corrêa, M., Camotim, D. (2010a). "A large displacement and finite rotation thin-walled beam formulation including cross-section deformation." *Computer Methods in Applied Mechanics and Engineering*, 199 (23-24) 1627-1643.

Gonçalves, R., Ritto-Corrêa, M., Camotim, D. (2010b). "A New Approach to the Calculation of Cross-Section Deformation Modes in the Framework of Generalized Beam Theory." *Computational Mechanics* 46(5) 759-781.

Gonçalves, R., Ritto-Corrêa, M., Camotim, D. (2011). "Incorporation of wall finite relative rotations in a geometrically exact thin-walled beam element." *Computational Mechanics*, 48(2) 229-244.

Gonçalves, R., Camotim, D. (2012). "Geometrically Non-Linear Generalised Beam Theory for Elastoplastic Thin-Walled Metal Members." *Thin-Walled Structures*, 51 121-129.

Gonçalves, R., Bebiano, R., Camotim, D. (2014). "On the Shear Deformation Modes in the Framework of Generalised Beam Theory." *Thin-Walled Structures*, 84 325-334.

Gonçalves, R. (2016). "A shell-like stress resultant approach for elastoplastic geometrically exact thin-walled beam finite elements." *Thin-Walled Structures* 103 263-272.
Gonçalves, R. (2019). "An assessment of the lateral-torsional buckling and post-buckling behaviour of steel I-section beams using a geometrically exact beam finite element." *Thin-Walled Structures* 143 106222 (15 pages).
Gruttmann, F. Sauer, R. Wagner, W. (1998). "A geometrical nonlinear eccentric 3D-beam element with arbitrary cross-sections." *Computer Methods in Applied Mechanics and Engineering*, 160 383-400.
Gruttmann, F., Sauer, R., Wagner, W. (2000). "Theory and numerics of three-dimensional beams with elastoplastic material behavior." *International Journal for Numerical Methods in Engineering*, 48 1675-1702.
Klinkel, S., Govindjee, S. (2003). "Anisotropic bending-torsion coupling for warping in a non-linear beam." *Computational Mechanics*, 31 78-87.
Martins, A., Camotim, D., Gonçalves, R., Dinis, P. (2018). "Enhanced geometrically non-linear Generalized Beam Theory (GBT) formulation: derivation, numerical implementation and illustration." *ASCE Journal of Engineering Mechanics*, 144(6), 04018036.
MATLAB (2010), version 7.10.0 (R2010a), *The MathWorks Inc*., Massachusetts.
Pignataro, M., Ruta, G. (2002). "Coupled instabilities in thin-walled beams: a qualitative approach." *European Journal of Mechanics A/Solids*, 22 139-149.
Peres, N., Gonçalves, R., Camotim, D. (2016). "First-order Generalised Beam Theory for curved thin-walled members with circular axis." *Thin-Walled Structures*, 107 345-361.
Peres, N., Gonçalves, R., Camotim, D. (2018a). "GBT-based cross-section deformation modes for curved thin-walled members with circular axis." *Thin-Walled Structures*, 127 769-780.
Peres, N., Gonçalves, R., Camotim, D. (2018b). "Application of Generalised Beam Theory to curved members with circular axis." *Stahlbau* 87(4) 345-354.
Peres, N., Gonçalves, R., Camotim, D. (2020). "A GBT-based mixed finite element for curved thin-walled members with circular axis." *Thin-Walled Structures*, 146 106462.
Petrov, E., Géradin, M. (1998). "Finite element theory for curved and twisted beams based on exact solutions for three-dimensional solids, Part 1: Beam concept and geometrically exact nonlinear formulation." *Computer Methods in Applied Mechanics and Engineering*, 165 43-92.
Pimenta, P., Campello, E. (2003). "A fully nonlinear multi-parameter rod model incorporating cross-sectional in-plane changes and out-of-plane warping." *Latin American Journal of Solids and Structures*, 1 (1) 119-140.
Reissner, E. (1972). "On one-dimensional finite-strain beam theory: the plane problem." *Journal of Applied Mathematics and Physics (ZAMP)*, 23 795-804.
Ritto-Corrêa, M., Camotim, D. (2002). "On the differentiation of the Rodrigues formula and its significance for the vector-like parameterization of Reissner-Simo beam theory." *International Journal for Numerical Methods in Engineering*, 55 (9) 1005-1032.
Ritto-Corrêa, M. (2004). *Structural analysis of frames: towards a geometrically exact, kinematically complete and materially non-linear theory.* PhD Thesis, IST/UTL (in Portuguese).
Rizzi, N., Tatone, A. (1996). "Nonstandard models for thin-walled beams with a view to applications." *Journal of Applied Mechanics (ASME)*, 63 399-403.
Simo, J. (1985). "A finite strain beam formulation. The three-dimensional dynamic problem, Part I." *Computer Methods in Applied Mechanics and Engineering*, 49 55-70.
Simo, J., Vu-Quoc, L., (1991). "A geometrically-exact rod model incorporating shear and torsion-warping deformation." *International Journal of Solids and Structures*, 27 (3) 371-393.